A needlet ILC analysis of WMAP 7-year polarisation data: CMB polarisation power spectra

Soumen Basak⋆, Jacques Delabrouille†
CNRS & Université Paris Diderot, Laboratoire APC, 10 rue Alice Domon et Léonie Duquet, 75205 Paris Cedex 13, France

2 March 2013

ABSTRACT

We estimate Cosmic Microwave Background (CMB) polarisation power spectra, and temperature-polarisation cross-spectra, from 7-year data of the Wilkinson Microwave Anisotropy Probe (WMAP). Foreground cleaning is implemented using needlet decompositions of sky maps for all WMAP channels, to produce maps for CMB temperature anisotropies (T-mode) and polarisation (E-mode and B-mode), for seven different years of observation. Power spectra are computed using a pixel-weighted scheme, from averages of independent cross-power estimates using foreground-cleaned maps for the different years. Error bars are estimated from the scatter of all possible independent measurements of the band-averaged power spectra, and hence are independent of any detailed model of the WMAP noise.

Our analysis technique yields a measurement of the EE spectrum on scales larger than about half a degree, that has smaller error bars than previous estimates and is in excellent agreement with theoretical expectations from the current concordance cosmological model. By comparison, the publicly available WMAP EE power spectrum is higher on average (and significantly higher than the expected EE spectrum from the current concordance best fit cosmological model), although individual data points are compatible with ours within quoted errors. Our TE and TB measurements are also in good agreement overall with the WMAP ones, but our estimated error bars are smaller. Their compatibility with the theoretical expectations, however, is not quite as good on average as for EE, as some data points are off by a few standard deviations. The upcoming Planck observations will help determine whether these data points are discrepant by reason of unmodelled residual systematics or foreground contamination, or indicate a tension in the best fit cosmological model. The EB and BB power spectra obtained in our analysis are compatible with zero, as expected for a standard cosmological model with low tensor to scalar ratio.

Key words: methods: data analysis – cosmic background radiation

1 INTRODUCTION

The Cosmic Microwave Background (CMB), relic radiation emitted when our Universe was about 380,000 years old, provides direct information about the origin and history of cosmic structure. Hence, the current understanding of cosmological evolution is heavily based on observations of the CMB. Over the last two decades, many experiments have accumulated observations on its temperature anisotropies, imprints of the original density perturbations that later on gave rise to the large scale structures observable today. Two very successful space missions,

the Cosmic Background Explorer (COBE, Bennett et al. 1996), and the Wilkinson Microwave Anisotropy Probe (WMAP, Bennett et al. 2003), complemented by several ground-based and balloon-borne experiments, such as CAT (Baker et al. 1999), Boomerang (de Bernardis et al. 2000), Maxima (Hanany et al. 2000), Archeops (Benoît et al. 2003a,b), CBI (Pearson et al. 2003), VSA (Dickinson et al. 2004; Rebolo et al. 2004), ACBAR (Reichardt et al. 2009), ACT (Das et al. 2011a,b), and SPT (Keisler et al. 2011), to mention just a few, have measured the CMB temperature anisotropies at various angular scales and at various wavelengths. The CMB angular power spectra measured by these experiments agree remarkably well, and strongly support a present 'concordance' cosmological model in which the Universe is spatially flat, with an energy density domi-

⋆ E-mail: basak@apc.univ-paris7.fr
† E-mail: delabrouille@apc.univ-paris7.fr

nated by the presence of about 70% dark energy and about 30% matter, and in which structure forms from gravitational collapse of primordial adiabatic perturbations in the density of the cosmological fluid. At present, this model does not require the additional admixture of primordial tensor perturbations (gravitational waves), although cosmological scenarios generically predict their existence. The observed CMB anisotropies are connected to the state of the cosmological fluid at recombination in a way that depends on a small set of parameters specific of the cosmological model. CMB observations are of prime importance for constraining these parameters of the model, as well as for testing its internal consistency.

Temperature anisotropies alone, however, do not provide the complete picture of the Universe. Independent information is needed to lift degeneracies between cosmological parameter sets compatible with the CMB temperature power spectrum. Other cosmological probes such as the direct measurement of the present expansion rate (Freedman et al. 2001), the observation of the expansion history with supernova (Perlmutter et al. 1999; Astier et al. 2006; Guy et al. 2010), or baryonic oscillations traced by the distribution of galaxies (Eisenstein et al. 2005), provide complementary constraints (Seljak, Slosar, & McDonald 2006).

On the side of the CMB itself, additional information are obtained by measuring CMB polarisation. The CMB is indeed partially polarised due to Thomson scattering of quadrupolar distribution of photons on free electrons at the time of recombination (Rees 1968), at a redshift z_{rec} of about 1100. Large scale polarisation also arises from the scattering of CMB photons on free electrons after reionisation of the Universe at much lower redshift ($z_{reion} < 10$). CMB polarisation is an additional observable, which helps disentangling Sachs-Wolfe from Doppler contributions to the anisotropies, makes possible the estimation of individual contributions to the power spectra from scalar and tensor perturbations, and also helps constraining the epoch of reionisation. The amplitude of the polarisation, however, is significantly lower than that of temperature anisotropies, which makes its precise characterisation challenging.

CMB polarisation was first detected at sub-degree angular scales by the DASI ground-based interferometer (Leitch et al. 2005). It was subsequently measured by Boomerang (Montroy et al. 2006; Piacentini et al. 2006), Maxipol (Wu et al. 2007), CBI (Sievers et al. 2007), CAPMAP (Bischoff et al. 2008), QUaD (Pryke et al. 2009; Brown et al. 2009), BICEP (Chiang et al. 2010), QUIET (QUIET Collaboration et al. 2011), and the Wilkinson Microwave Anisotropy Probe (WMAP, Nolta et al. 2009; Larson et al. 2011).

The level of the CMB polarisation (at most a few per cent, depending on the angular scale), however, makes it easily contaminated by foreground emissions from both the Galaxy and extragalactic sources. Galactic emission, in particular, can be polarised at the level of a few tens of per cent, i.e. ten times more than CMB anisotropies. The signal to foreground ratio is thus less favourable for polarisation than for intensity, in particular on large angular scales where Galactic synchrotron and dust emissions are strong. Contamination by foregrounds would result in CMB polar-

isation power spectra larger than predicted by the current concordance cosmological model.

Hence, contamination from polarised foreground signals has to be removed as much as possible for the accurate measurement of the temperature and polarisation angular power spectrum of the CMB. The effectiveness of a foreground cleaning technique is typically significantly improved by the use of prior knowledge of the emission properties of the contaminant (such as the frequency dependence, typical angular power spectrum of its emission, or availability of external templates). However, since the properties of foreground contamination are poorly known for polarisation (and, in particular, no good template of polarised foregrounds is presently available), it is particularly crucial to develop and use data analysis tools that use only the minimum possible prior assumptions about foreground polarisation.

Among the possible methods for CMB cleaning, the so-called Internal Linear Combination (ILC) method, first proposed for foreground cleaning in the analysis of COBE-DMR data (Bennett et al. 1992), and discussed subsequently by many authors (see, e.g., Tegmark 1998; Delabrouille & Cardoso 2009), is a simple and effective way to combine multifrequency observations to extract the CMB while rejecting contamination by superimposed foreground signals. This method is based on two reasonably safe assumptions. The first is that the amplitude of CMB emission is frequency independent in thermodynamic units, i.e. that the CMB emission law scales in frequency as the derivative of the blackbody spectrum of the cosmic background. The second is that CMB fluctuations are not correlated to foreground signals. Under these assumptions, the ILC estimates the CMB as a linear combination of sky maps such that the variance of the estimate is minimum, while preserving unit response to the CMB (see, however, the appendix of Delabrouille et al. (2009) for a discussion of second order corrections and biases, and Dick, Remazeilles, & Delabrouille (2010) for a discussion of the impact of calibration errors).

Component separation with an ILC method can be straightforwardly implemented either in real space or in harmonic space (Tegmark, de Oliveira-Costa, & Hamilton 2003; Eriksen et al. 2004; Saha, Jain & Souradeep 2006; Souradeep, Saha., Jain 2006; Saha, Prunet, Jain & Souradeep 2008; Saha 2011; Souradeep 2011). Here, as in our previous work (Delabrouille et al. 2009; Basak & Delabrouille 2012), we instead implement the ILC on a frame of spherical wavelets, called needlets. This special type of wavelets on the sphere provides good localisation in both pixel space and harmonic space because they have compact support in the harmonic domain, while still being very well localised in the pixel domain (Narcowich, Petrushev & Ward 2006; Marinucci et al. 2008; Guilloux, Fay, & Cardoso 2009). Needlets have already been used in various analyses of WMAP data besides component separation and power spectrum estimation, for instance by Pietrobon et al. (2008) to detect features in the CMB, and by Rudjord et al. (2009) to put limits on the non-gaussianity parameter f_{NL}.

Recently, we have used a needlet ILC on WMAP 7-year data to obtain an estimate of the CMB temperature angular power spectrum (Basak & Delabrouille 2012). In the present paper, as a natural extension to this work, we address the

problem of measuring as precisely as possible the CMB polarisation power spectra from WMAP 7-year observations.

The paper is organised as follows: In section 2 we describe the methodology to estimate the CMB using an ILC on wavelet decompositions of multi-frequency sky maps. The implementation of this on WMAP 7-year data, and the results for polarisation power spectra, are described in section 3 and section 4. We conclude in section 5.

2 NEEDLET ILC ESTIMATE OF CMB

A scalar field on the sphere such as CMB temperature anisotropies is conveniently expanded in usual spherical harmonics:

$$T(\hat{n}) = \sum_{l=0}^{\infty} \sum_{m=-l}^{l} T_{lm} Y_{lm}(\hat{n}) \tag{1}$$

The CMB polarisation field is usually specified using the Stokes parameters, Q and U, with respect to a particular choice of a coordinate system on the sky in relation to which the linear polarisation is defined. One can conveniently combine the Stokes parameters into the single complex quantity, $P_{\pm} = Q \pm iU$. Due to its rotation properties, one may expand $P(\hat{n})$ in terms of spin-2 spherical harmonics, $_{\pm 2}Y_{lm}(\hat{n})$ (Goldberg et al. 1967), as:

$$P_{\pm}(\hat{n}) = \sum_{l=0}^{\infty} \sum_{m=-l}^{l} P_{\pm 2, lm} \,_{\pm 2}Y_{lm}(\hat{n}). \tag{2}$$

The description of CMB polarisation, however, traditionally makes use of two scalar fields that are independent of how the coordinate system is oriented, and are related to the Stokes parameters by a non-local transformation (Zaldarriaga & Seljak 1997; Kamionkowski, Kosowsky, & Stebbins 1997). One of the fields, traditionally denoted as E, has even parity, whereas the other one, B, has odd parity (and hence is pseudo-scalar, rather than scalar). In harmonic space, the E and B modes of CMB polarisation are related to the complex polarisation fields $P_{\pm}$ as,

$$P_{+2, lm} = -(E_{lm} + iB_{lm}) \tag{3}$$

and

$$P_{-2, lm} = -(E_{lm} - iB_{lm}). \tag{4}$$

Hence, one can fully characterise CMB anisotropies using three Gaussianly distributed random scalar fields (T, E and B), without loss of information. In the following, maps of Q and U are systematically converted into maps of E and B by expansion onto spin-2 spherical harmonics, followed by an inverse spherical harmonic transform for E_{lm} and B_{lm} independently.

2.1 The CMB data model

Denote $X^{\mathrm{OBS},c}(\hat{n})$, ($X = T, E, B$) full-sky, multi-frequency temperature anisotropy and polarisation maps of the sky in n_c different frequency bands (channels), such as those provided by WMAP. The observed signals $X^{\mathrm{OBS},c}(\hat{n})$ in channel

c can be modelled as,

$$X^{\mathrm{OBS},c}(\hat{n}) = \int_{\hat{n}'} d\Omega_{\hat{n}'} \, b^c(\hat{n}.\hat{n}') \, X^{\mathrm{SIG},c}(\hat{n}') + X^{\mathrm{N},c}(\hat{n}) \tag{5}$$

where $X^{\mathrm{SIG},c}(\hat{n})$ is the signal (sky) component, itself decomposed in the sum of CMB and foreground components,

$$X^{\mathrm{SIG},c}(\hat{n}) = a^c \, X^{\mathrm{CMB}}(\hat{n}) + X^{\mathrm{FG},c}(\hat{n}), \tag{6}$$

a^c being the CMB calibration coefficient for the channel c. Up to calibration uncertainties, $a^c = 1$ for all WMAP channels. If, in addition to WMAP data, we use external data sets which serve as foreground templates to help foreground subtraction, as done in the present work, the coefficients a^c vanish for such data sets (i.e. the ancillary maps contain no CMB anisotropies).

The beam function $b^c(\hat{n}.\hat{n}')$, represents the smoothing of the signal due to the finite resolution of the observations. Assuming for simplicity that the beams are circularly symmetric (a good approximation for WMAP data), $b^c(\hat{n}.\hat{n}')$ depends only on the angle $\theta = \cos^{-1}(\hat{n}.\hat{n}')$ between the directions $\hat{n}$ and $\hat{n}'$, and can be expanded in terms of Legendre polynomials,

$$b^c(\hat{n}.\hat{n}') = \sum_{l=0}^{\infty} \frac{2l+1}{4\pi} b_l^c P_l(\hat{n}.\hat{n}'). \tag{7}$$

The last term, $X^{\mathrm{N},c}(\hat{n})$, in equation 5 represents the detector noise in channel c, and is not affected by the beam function. For a spherically symmetric beam, equation 5 can be recast straightforwardly in the spherical harmonic representation, as:

$$X_{lm}^{\mathrm{OBS},c} = a^c \, b_l^c \, X_{lm}^{\mathrm{CMB}} + b_l^c \, X_{lm}^{\mathrm{FG},c} + X_{lm}^{\mathrm{N},c} \tag{8}$$

where X_{lm} stands for the three modes T_{lm}, E_{lm} and B_{lm} of temperature and polarisation in harmonic space.

2.2 Implementation of the needlet transform

Considering that each channel observes the sky at a different resolution, the maps are first convolved/deconvolved, in harmonic space, to the same resolution:

$$X_{lm}^c = \frac{b_l}{b_l^c} \, X_{lm}^{\mathrm{OBS},c}. \tag{9}$$

Each of these maps X_{lm}^c is then decomposed into a set of filtered maps $X_{lm}^{c,j}$ represented by the spherical harmonic coefficients,

$$X_{lm}^{c,j} = h_l^j X_{lm}^c, \tag{10}$$

where the filters h_l^j, serving for localisation in the harmonic space, are chosen in such a way that

$$\sum_j \left(h_l^j \right)^2 = 1. \tag{11}$$

The reconstruction of the original maps X_{lm}^c from the collection of the filtered maps $X_{lm}^{c,j}$, representing each a different scale, is performed using the same set of filters. In terms of h_l^j, the spherical needlets are defined as,

$$\Psi_{jk}(\hat{n}) = \sqrt{\lambda_{jk}} \sum_{l=0}^{l_{\max}} \sum_{m=-l}^{l} h_l^j Y_{lm}^*(\hat{n}) Y_{lm}(\hat{\xi}_{jk}), \tag{12}$$

where $\{\xi_{jk}\}$ denote a set of cubature points on the sphere for scale j. In practice, we identify these points with the pixel centres in the HEALPix pixelisation scheme (Górski et al. 2005). Each index k corresponds to a particular HEALPix pixel, at a resolution parameter $\mathtt{nside}(j)$ specific to that scale j. The cubature weights λ_{jk} are inversely proportional to the number N_j of pixels used for the needlet decomposition, i.e. $\lambda_{jk} = \frac{4\pi}{N_j}$. The needlet coefficients for CMB fields $X(\hat{n})$ are denoted as,

$$
\begin{aligned}
\beta_{jk}^X &= \int_{S^2} X(\hat{n})\,\Psi_{jk}(\hat{n})\,d\Omega_{\hat{n}} \\
&= \sqrt{\lambda_{jk}} \sum_{l=0}^{l_{\max}} \sum_{m=-l}^{l} h_l^j\,b_l\,X_{lm}\,Y_{lm}(\xi_{jk}).
\end{aligned}
\tag{13}
$$

The linearity of the needlet decomposition implies that the needlet coefficients β_{jk}^c corresponding to the filtered map obtained from the harmonic coefficients $X_{lm}^{c,j}$ are a linear combination of the needlet coefficients of individual components and noise at HEALPix grid points ξ_{jk}:

$$
\beta_{jk}^{X,c} = a^c\,\beta_{jk}^{\mathrm{CMB}} + \beta_{jk}^{\mathrm{FG},c} + \beta_{jk}^{\mathrm{N},c}
\tag{14}
$$

where,

$$
\begin{aligned}
\beta_{jk}^{\mathrm{CMB}} &= \sqrt{\lambda_{jk}} \sum_{l=0}^{l_{\max}} \sum_{m=-l}^{l} h_l^j\,b_l\,X_{lm}^{\mathrm{CMB}}\,Y_{lm}(\xi_{jk}) \\
\beta_{jk}^{\mathrm{FG},c} &= \sqrt{\lambda_{jk}} \sum_{l=0}^{l_{\max}} \sum_{m=-l}^{l} h_l^j\,b_l\,X_{lm}^{\mathrm{FG},c}\,Y_{lm}(\xi_{jk}) \\
\beta_{jk}^{\mathrm{N},c} &= \sqrt{\lambda_{jk}} \sum_{l=0}^{l_{\max}} \sum_{m=-l}^{l} h_l^j\,\frac{b_l}{b_l^c}\,X_{lm}^{\mathrm{N},c}\,Y_{lm}(\xi_{jk})
\end{aligned}
\tag{15}
$$

2.3 Implementation of the needlet ILC

The ILC estimate of needlet coefficients of the cleaned map is obtained as a linearly weighted sum of the needlet coefficients β_{jk}^c,

$$
\beta_{jk}^{\mathrm{NILC}} = \sum_{c=1}^{n_c} \omega_{jk}^c\,\beta_{jk}^{X,c}
\tag{16}
$$

where ω_{jk}^c is the needlet weight for scale j and frequency channel c, at the pixel k of the HEALPix representation of the needlet coefficients for that scale. Under the assumption of decorrelation between CMB and foregrounds, and between CMB and noise, the empirical variance of the error is minimum when the empirical variance of the ILC map itself is minimum. The condition for preserving the CMB signal during the cleaning is encoded as the constraint:

$$
\sum_{c=1}^{n_c} a^c\,\omega_{jk}^c = 1.
\tag{17}
$$

The resulting needlet ILC weights $\widehat{\omega}_{jk}^c$ that minimise the variance of the reconstructed CMB, subject to the constraint that the CMB is preserved, are expressed as:

$$
\widehat{\omega}_{jk}^c = \frac{\sum_{c'} \left[\widehat{R}_{jk}^{-1}\right]^{cc'} a^{c'}}{\sum_c \sum_{c'} a^c \left[\widehat{R}_{jk}^{-1}\right]^{cc'} a^{c'}},
\tag{18}
$$

where indices c and c' of elements of the matrix $\left[\widehat{R}_{jk}^{-1}\right]$ and of the vectors $\widehat{\omega}_{jk}$ and a are written down explicitly for clarity. More compactly, we have:

$$
\widehat{\omega}_{jk} = \frac{\left[\widehat{R}_{jk}^{-1}\right] a}{a^T \left[\widehat{R}_{jk}^{-1}\right] a},
\tag{19}
$$

where $\widehat{\omega}_{jk}$ is the vector of ILC weights to be applied to the needled coefficients of all input observations at scale j and in pixel k, a is the CMB 'mixing vector' (a vector of n_c entries all equal to unity for inputs in thermodynamic temperature), and $\left[\widehat{R}_{jk}^{-1}\right]$ an estimate of the inverse covariance of the needlet coefficients of the n_c observations at pixel k of scale j.

The NILC estimate of the cleaned CMB needlet coefficients is:

$$
\beta_{jk}^{\mathrm{NILC}} = \beta_{jk}^{\mathrm{CMB}} + \sum_c \widehat{\omega}_{jk}^c \left(\beta_{jk}^{\mathrm{FG},c} + \beta_{jk}^{\mathrm{N},c}\right).
\tag{20}
$$

The elements of the covariance matrix for scale j at pixel k, $R_{jk}^{cc'} = \left\langle \beta_{jk}^c \beta_{jk}^{c'} \right\rangle$, are obtained each as an average of the product of the relevant computed needlet coefficients over some space domain $\mathcal{D}_k$ centred at k. In practice, they are computed as

$$
\widehat{R}_{X,jk}^{cc'} = \frac{1}{n_k} \sum_{k'} w_j(k,k')\,\beta_{jk}^{X,c}\,\beta_{jk}^{X,c'},
\tag{21}
$$

where the weights $w_j(k,k')$ define the domain $\mathcal{D}_k$. A sensible choice is for instance $w_j(k,k') = 1$ for k' closer to k than some limit angle, and $w_j(k,k') = 0$ elsewhere, or alternatively, $w_j(k,k')$ shaped as a Gaussian beam of some given size that depends on the scale j (which is what we do here).

Finally, the NILC estimate of the cleaned CMB map can be reconstructed from cleaned CMB needlet coefficients using the same set of filters that was used to decompose the original maps into their needlet coefficients. The NILC CMB temperature map is then

$$
X^{\mathrm{NILC}}(\hat{n}) = \sum_{lm} X_{lm}^{\mathrm{NILC}} Y_{lm}(\hat{n})
\tag{22}
$$

with

$$
X_{lm}^{\mathrm{NILC}} = b_l\,X_{lm}^{\mathrm{CMB}} + X_{lm}^{\mathrm{RFG}} + X_{lm}^{\mathrm{RN}},
\tag{23}
$$

where the harmonic coefficients residual foreground (X_{lm}^{RFG}) and residual noise (X_{lm}^{RN}) are given by:

$$
X_{lm}^{\mathrm{RFG}} = \sum_j \sum_k \sqrt{\lambda_{jk}}\,\beta_{jk}^{\mathrm{RFG}}\,h_l^j\,Y_{lm}(\xi_{jk})
\tag{24}
$$

and

$$
X_{lm}^{\mathrm{RN}} = \sum_j \sum_k \sqrt{\lambda_{jk}}\,\beta_{jk}^{\mathrm{RN}}\,h_l^j\,Y_{lm}(\xi_{jk}).
\tag{25}
$$

Equations 22 and 23 imply that the NILC estimate of CMB contains some residual foreground and noise contamination.

3 WMAP 7-YEAR NEEDLET ILC MAP

The WMAP satellite has observed the sky in five frequency bands denoted K, Ka, Q, V and W, centred at 23, 33, 41, 61 and 94 GHz respectively. After 7 years of observation,

Table 1. List of needlet bands used in the present analysis.

Band index	l_{min}	l_{peak}	l_{max}	nside
1	0	0	50	32
2	0	50	100	64
3	50	100	150	128
4	100	150	250	128
5	150	250	350	256
6	250	350	550	512
7	350	550	650	512
8	550	650	800	512
9	650	800	1000	512

Figure 1. Needlet bands used in the present analysis. The black line shows the normalisation of the needlet bands, i.e. the total filter applied to the original map after needlet decomposition and synthesis of the output map from needlet coefficients.
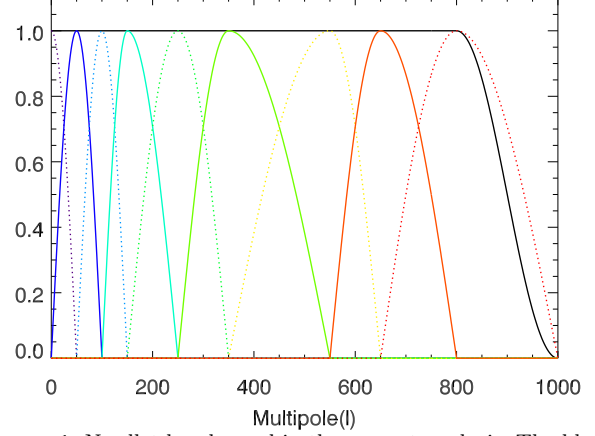
the released data includes temperature anisotropy and polarisation maps obtained with ten difference assemblies, for 7 individual years. One map is available, per year, for each of the K and Ka bands, two for the Q band, two for the V band and four for the W band. These sky maps are sampled using the HEALPix pixelisation scheme at a resolution level (nside = 512), corresponding to approximately 3 million sky pixels.

We work on band-averaged maps of T, E and B for the five frequency bands, complemented, for temperature only, by three foreground templates (dust at 100 microns, as obtained by Schlegel, Finkbeiner, & Davis (1998), the 408 MHz synchrotron map of Haslam et al. (1981), and the composite all-sky H-alpha map of Finkbeiner (2003)). All sky maps are convolved/deconvolved in harmonic space, to a common beam resolution (corresponding to that of the W frequency channel of WMAP 7-year release).

Each of these maps is then decomposed into a set of needlet coefficients. For each scale j, needlet coefficients of a given map are stored in the format of a single HEALPix map at degraded resolution. The filters h_l^j used to compute filtered maps are shaped as follows:

$$
h_l^j = \begin{cases} \cos\left[\left(\dfrac{l_{peak}^j - l}{l_{peak}^j - l_{min}^j}\right)\dfrac{\pi}{2}\right] & \text{for } l_{min}^j \leqslant l < l_{peak}^j, \\[2em] 1 & \text{for } l = l_{peak}, \\[2em] \cos\left[\left(\dfrac{l - l_{peak}^j}{l_{max}^j - l_{peak}^j}\right)\dfrac{\pi}{2}\right] & \text{for } l_{peak}^j < l \leqslant l_{max}^j \end{cases}
$$

For each scale j, the filter has compact support between the multipoles l_{min}^j and l_{max}^j with a peak at l_{peak}^j (see figure 1 and table 1). The needlet coefficients β_{jk}^X are computed from these filtered maps on HEALPix grid points ξ_{jk} with resolution parameter nside equal to the smallest power of 2 larger than $l_{max}^j/2$. The estimates of needlet coefficients covariance matrices, for each scale j, are computed by smoothing maps of products of needlet coefficient $\beta_{jk}^c \beta_{jk}^{c'}$ with Gaussian beams. In this way, an estimate of needlet covariances at each point k is obtained as a local, weighted average of nearby needlet coefficient products. The full width at half maximum (FWHM) of each of the Gaussian windows used for this purpose is chosen to ensure the computation of the statistics by averaging about 1200 samples or more, resulting from a trade-off between the localisation of the estimates (which requires small windows), and the accuracy of the es-

timate (which require large windows). Choosing a smaller FWHM results in inaccuracy in the covariance estimates, and hence ILC bias. Choosing a larger FWHM results in less localisation, and hence loss of effectiveness of the needlet approach.

Using these covariance matrices, ILC weights are computed for each of T, E and B, for each scale j and for each pixel k of the needlet representation at scale j. For each of T, E and B, a full sky CMB map, at the resolution of the WMAP W channel, is synthesised from the NILC needlet coefficients.

4   WMAP 7-YEAR NEEDLET ILC SPECTRUM

As already mentioned above, the foreground-cleaned maps of T, E and B obtained in this way are not fully exempt from contamination by residual foregrounds and noise. The recovered CMB map (T, Q and U) at 60 arcmin resolution is displayed in figure 2. Residual foreground contamination, albeit small, is visible along a narrow strip on the Galactic plane of the maps. Noise contamination is seen from the larger variance of the polarisation maps away from the ecliptic poles.

4.1   Minimisation of the impact of noise

Noise biasing in our estimated power spectra is avoided by producing, for each of T, E and B, an independent CMB map for each of the 7 individual years of observation, and computing the CMB power spectra exclusively from cross-products between maps from different years. Each data point in our spectra is thus obtained as an average of 21 possible cross-year spectra. All maps, however, are obtained using the same set of needlet weights, determined using the co-added 7 year observations.

4.2   Minimisation of the impact of foregrounds

Unlike the residual noise, the residual foreground emission in each of 7 cleaned maps is the same, as each map observes
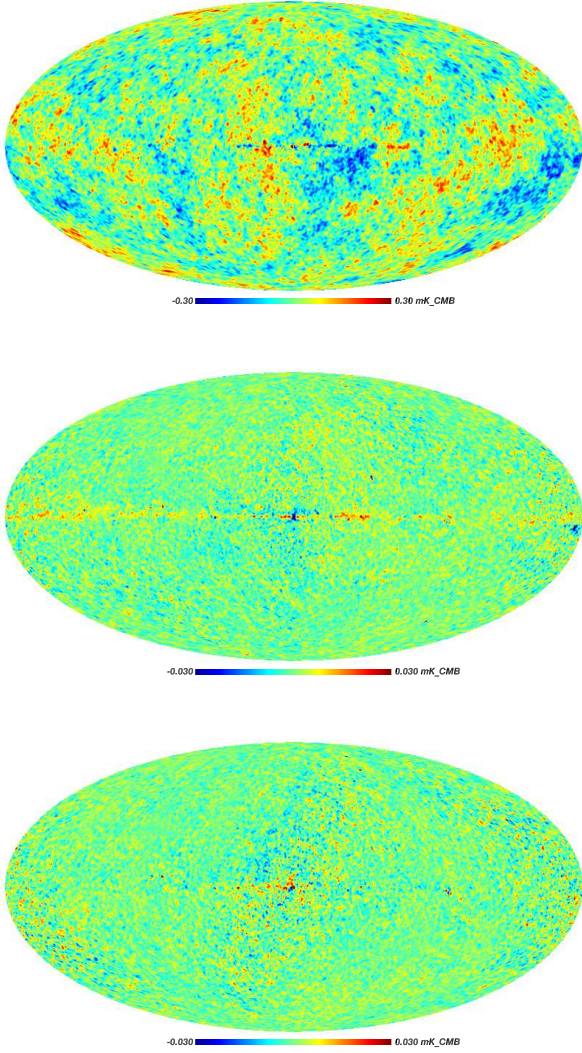
Figure 2. The NILC estimate of temperature anisotropies(top) and, Stokes parameters Q (middle) and U (bottom) of CMB obtained by implementing the NILC on the 7-year band average maps, at nside = 512 and degraded to 60 arcmin resolution.

Figure 3. Apodisation kernel for Galactic mask used in our analysis

the same sky emission, and is produced using the same linear combination for all years.

For safety, we use a conservative mask for estimating CMB angular power spectra, that combines the point source mask provided by the WMAP collaboration with an apodised Galactic mask, applied directly on the CMB maps after the needlet ILC. We choose this option (rather than masking before the ILC) so that we produce full sky CMB maps that can also be used for other purposes than power spectrum estimation.

The Galactic mask $M_{\bar{\theta}_r,\bar{\theta}_w}$ used in practice is:

$$
M_{\bar{\theta}_r,\bar{\theta}_w}(\theta,\phi) = \begin{cases} 0 & \text{for } 0° \leqslant |\bar{\theta}| < \bar{\theta}_r, \\[2mm] \sin^2\left[\left(\frac{\bar{\theta}-\bar{\theta}_r}{\theta_w}\right)\frac{\pi}{2}\right] & \text{for } \bar{\theta}_r \leqslant |\bar{\theta}| \leqslant \bar{\theta}_r + \bar{\theta}_w, \\[2mm] 1 & \text{for } |\bar{\theta}| > \bar{\theta}_r + \bar{\theta}_w \end{cases}
$$

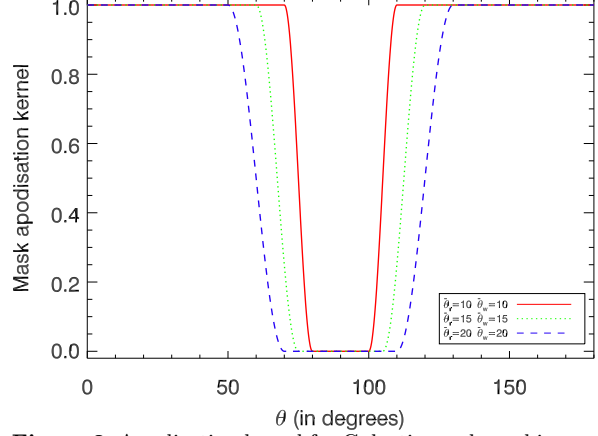We use $M_{10°,10°}$, $M_{15°,15°}$, $M_{20°,20°}$ to compute auto and cross angular power spectra involving T, E and B field of CMB respectively.

Finally, for power spectrum estimation, small gaps induced by the point source mask are filled-in by an interpolation procedure using the values of CMB anisotropies in the neighbouring unmasked pixels.

4.3   Impact of calibration errors

An important assumption of the ILC is that the frequency scaling of the CMB is known. However, calibration coefficients for each channel, which are a multiplicative factor for each frequency, introduce an uncertainty in the frequency scalings of the CMB component in the presence of calibration errors (Dick, Remazeilles, & Delabrouille 2010). This effect is particularly strong in the high signal to noise ratio regime. Considering the relatively low signal to noise of WMAP polarised maps, this issue can safely be ignored here.

Beam uncertainties induce similar biases as calibration uncertainties, except that these biases are scale dependent. Here again, such biases are not the main source of error in our final polarisation spectra, as their impact is small in comparison to the uncertainties due to instrumental noise for polarisation measurements with WMAP.

These issues connected to the exact response of the detectors, however, will require specific attention with upcoming more sensitive observations of the polarised CMB, if our method is to be used for the analysis of these future data sets.

4.4   Noise-weighting

Residual noise in our CMB maps is inhomogeneous, primarily because of non-uniform sky coverage, with higher number of observations in the directions of ecliptic poles and rings at $45°$ ecliptic latitude.

The estimation of band-averages of the CMB power spectrum (in bins of l), results in lowering the effective resolution in harmonic space (as compared to computing power spectra for every single value of l). This results in the capacity to measure the bin-averaged power spectrum with some

Table 2. Comparison of our estimate of binned angular power spectrum of E-mode of CMB polarisation with that provided by WMAP team. The quantities tabulated are $D_l = l(l+1)C_l^{EE}/2\pi$ and $\Delta D_l = l(l+1)\Delta C_l^{EE}/2\pi$.

l	D_l^{nilc}	D_l^{wmap}	$\Delta D_l^{\mathrm{nilc}}$	$\Delta D_l^{\mathrm{wmap}}$
	(mK^2)	(mK^2)	(mK^2)	(mK^2)
4	1.362e-07	8.175e-08	7.768e-08	3.275e-08
15	5.874e-08	9.551e-08	5.609e-08	4.312e-08
36	5.385e-08	2.528e-07	1.033e-07	1.093e-07
74	4.346e-07	8.108e-07	1.689e-07	2.454e-07
124	1.275e-06	1.083e-06	4.130e-07	5.832e-07
174	1.117e-06	4.155e-07	9.204e-07	1.132e-06
224	1.074e-06	1.827e-06	1.625e-06	2.044e-06
274	4.690e-06	7.534e-06	2.702e-06	3.556e-06
324	1.531e-05	2.425e-05	5.272e-06	5.975e-06
374	2.724e-05	3.342e-05	8.263e-06	9.668e-06
424	1.624e-05	1.759e-05	1.691e-05	1.517e-05
474	2.451e-05	4.171e-05	1.641e-05	2.339e-05
549	-3.229e-05	1.141e-05	3.054e-05	3.209e-05
674	2.820e-05	7.206e-05	6.119e-05	7.273e-05

localisation in pixel space, and hence compute the band averaged power as weighted averages of local estimates. We take advantage of this opportunity and follow the general idea of the noise-weighting over needlet domains already performed in our previous analysis of WMAP intensity maps (Basak & Delabrouille 2012), also investigated for temperature in a method paper by Faÿ et al. (2008).

The contribution of instrumental noise, in each bin of l, at each location of the sky, is estimated using 100 independent realisations of the reconstruction of the CMB by the NILC. This local noise variance is then used to compute a weighted average of the band-averaged power, estimated locally from the covariance of maps filtered with the spectral window of interest. This method yields more precise estimates of CMB power spectra in those angular scales where residual noise dominates over residual foreground signal, a feature of particular interest for polarisation measurement on small scales, for which the noise is the main source of error.

Note that the apodised Galactic masks used in the power spectrum estimation (see equation (26) and figure 3), also act as effective weights over the the pixel space (with vanishing weights at the lowest Galactic latitudes).

We are using here the methodology already described in Basak & Delabrouille (2012). The adaptation for polarisation and cross spectra is straightforward, and we refer to our previous work for implementation details.

4.5 Results

We now present the estimated polarisation power spectra we obtain on the basis of WMAP 7 year observations. The error bars in our estimates include the total statistical error of the estimator (noise and cosmic variance terms).
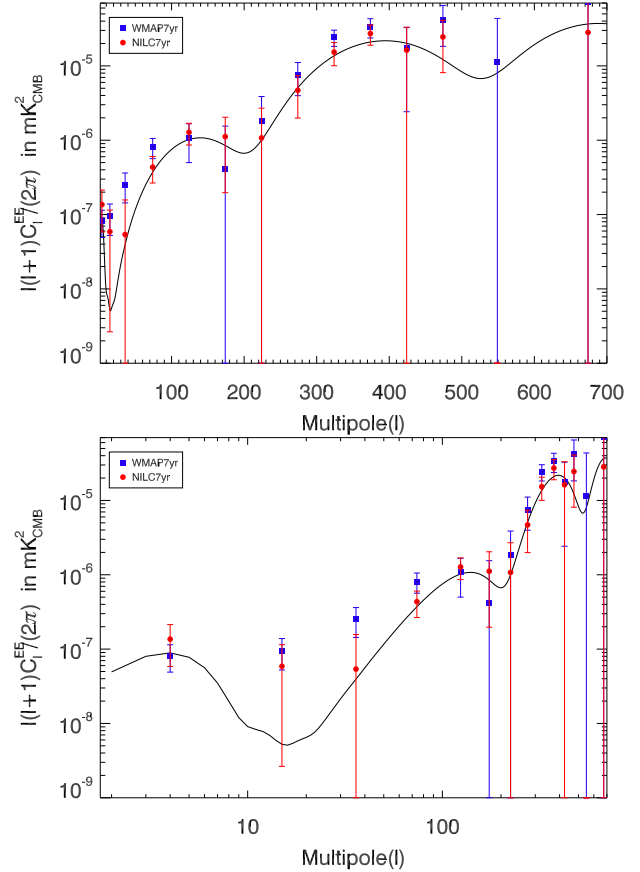

Figure 4. The red circles show the angular power spectrum of E-mode of CMB polarisation estimated using 7 years of observations of WMAP. The dark blue squares show the 7-year angular power spectrum of E-mode of CMB polarisation published by the WMAP collaboration. The solid black line shows the theoretical angular power spectrum for WMAP best-fit Λ-CDM model. The top panel uses a linear scale in the horizontal axis, and the bottom panel a logarithmic scale.

4.5.1 EE angular power spectrum

Figure 4 shows the estimated auto-angular power spectrum for the E-mode of CMB polarisation. Our result for E-mode CMB power is slightly higher than that obtained by WMAP collaboration[1] in the first bin (on very large angular scales, corresponding to $l = 4$), although the two are compatible within error bars (see table 2). Considering that we use a different mask, different methodology, and different weighting scheme, the small difference between the two measurements is not too surprising. In most of the rest of the scales, our measurements are lower than the WMAP result, and in better agreement with the theoretical expectations (assuming the concordance cosmological model is correct). The difference between our measurement and that of the WMAP team may point out that the latter could be biased by excess residual foreground contamination.

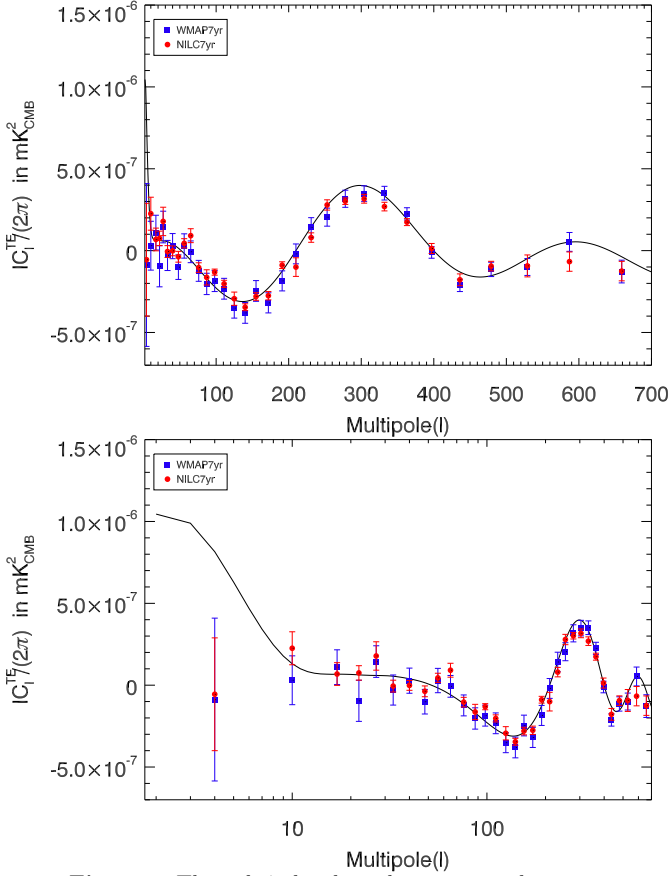[1] http://lambda.gsfc.nasa.gov/data/map/dr4/dcp/spectra/wmap_ee_spectrum_7yr

Table 3. Comparison of our estimate of binned cross-angular power spectrum of CMB temperature anisotropies (T-mode) and E-mode of CMB polarisation with that provided by WMAP team. The quantities tabulated are $D'_l = lC_l^{TE}/2\pi$ and $\Delta D'_l = l\Delta C_l^{TE}/2\pi$.

l	$D_l'^{,\mathrm{nilc}}$	$D_l'^{,\mathrm{wmap}}$	$\Delta D_l'^{,\mathrm{nilc}}$	$\Delta D_l'^{,\mathrm{wmap}}$
	(mK^2)	(mK^2)	(mK^2)	(mK^2)
4	-5.543e-08	-8.783e-08	3.445e-07	4.973e-07
10	2.256e-07	3.015e-08	1.006e-07	1.492e-07
17	6.819e-08	1.100e-07	6.946e-08	1.060e-07
22	7.488e-08	-9.548e-08	4.420e-08	1.257e-07
27	1.784e-07	1.443e-07	8.683e-08	9.661e-08
33	-5.565e-09	-2.954e-08	3.609e-08	9.197e-08
40	-1.288e-09	2.755e-08	3.003e-08	7.685e-08
48	-3.747e-08	-1.009e-07	3.294e-08	7.507e-08
56	4.466e-08	2.842e-08	2.823e-08	7.429e-08
65	9.132e-08	-7.147e-09	4.255e-08	6.643e-08
76	-1.035e-07	-1.235e-07	2.935e-08	6.398e-08
87	-1.634e-07	-2.033e-07	4.655e-08	6.520e-08
98	-1.314e-07	-1.860e-07	1.856e-08	6.404e-08
111	-2.030e-07	-2.329e-07	2.170e-08	6.345e-08
125	-2.938e-07	-3.512e-07	4.054e-08	6.117e-08
140	-3.458e-07	-3.804e-07	2.096e-08	6.336e-08
155	-2.802e-07	-2.463e-07	2.311e-08	6.333e-08
172	-2.753e-07	-3.191e-07	2.544e-08	6.145e-08
191	-8.883e-08	-1.848e-07	2.062e-08	6.126e-08
210	-1.006e-07	-1.997e-08	5.702e-08	6.067e-08
231	7.976e-08	1.418e-07	2.882e-08	5.951e-08
253	2.789e-07	2.045e-07	3.142e-08	5.508e-08
278	3.020e-07	3.167e-07	1.983e-08	5.223e-08
304	3.168e-07	3.487e-07	2.679e-08	4.749e-08
332	2.690e-07	3.510e-07	2.618e-08	4.169e-08
363	1.740e-07	2.244e-07	2.120e-08	3.762e-08
397	1.307e-08	-1.108e-08	3.060e-08	3.549e-08
436	-1.781e-07	-2.123e-07	3.602e-08	3.764e-08
479	-9.450e-08	-1.146e-07	2.937e-08	4.372e-08
529	-9.332e-08	-9.995e-08	6.702e-08	5.169e-08
587	-6.719e-08	5.319e-08	5.902e-08	5.758e-08
659	-1.251e-07	-1.278e-07	5.942e-08	6.950e-08

Figure 5. The red circles show the cross-angular power spectrum of CMB temperature anisotropies (T-mode) and E-mode of CMB polarisation estimated using 7 years of observation of WMAP. The dark blue squares show the 7-year angular power spectrum of E-mode of CMB polarisation published by the WMAP collaboration. The solid line shows the theoretical angular power spectrum for WMAP best-fit 'concordance' Λ-CDM model. The top panel uses a linear scale in the horizontal axis, and the bottom panel a logarithmic scale.

4.5.2   TE cross-spectrum

Figure 5 shows the estimated cross-angular power spectrum for temperature anisotropy of CMB and E-mode of CMB polarisation. The power spectrum obtained using our analysis agrees well with that provided by the WMAP collaboration and is in general consistent with the ΛCDM model for WMAP best-fit cosmological parameters. Our error bars, computed from the internal scatter of 21 individual measurements in each bin, are smaller than those provided by the WMAP collaboration[2]. We note, however, that four of our data points between $l = 50$ and $l = 120$ (at $l = 56$, 65, 98, 111) are significantly above the WMAP best fit model (up to ~ 4 standard deviations away) (see table 3). Whether this indicates that the WMAP best fit model is not a good fit to the observations, or that our error bars are impacted by un-modelled systematics, is at present not clear. It will be investigated further with upcoming data sets, such as those from the Planck mission.

We also note that our cross-spectrum estimate seems to be consistently slightly lower on average than that of the WMAP collaboration, as well as the theoretical expectation from the concordance model, around the peak at $l = 300$. Individual points agree within error bars, but there seems to be a systematic difference that remains to be explained.

4.5.3   TB cross-spectrum

Our result for the TB cross-spectrum, compared to the WMAP collaboration one,[3] is shown in figure 6. Theoretically, this cross-spectrum is supposed to vanish (to preserve the parity symmetry), and significant departure from zero would be the sign of either unknown systematics in the measurement (including residual foregrounds), or new physics.

Although our estimated TB cross-power spectrum is in general in good agreement with the expectation of a vanishing cross-power, a few of the data points shows significant

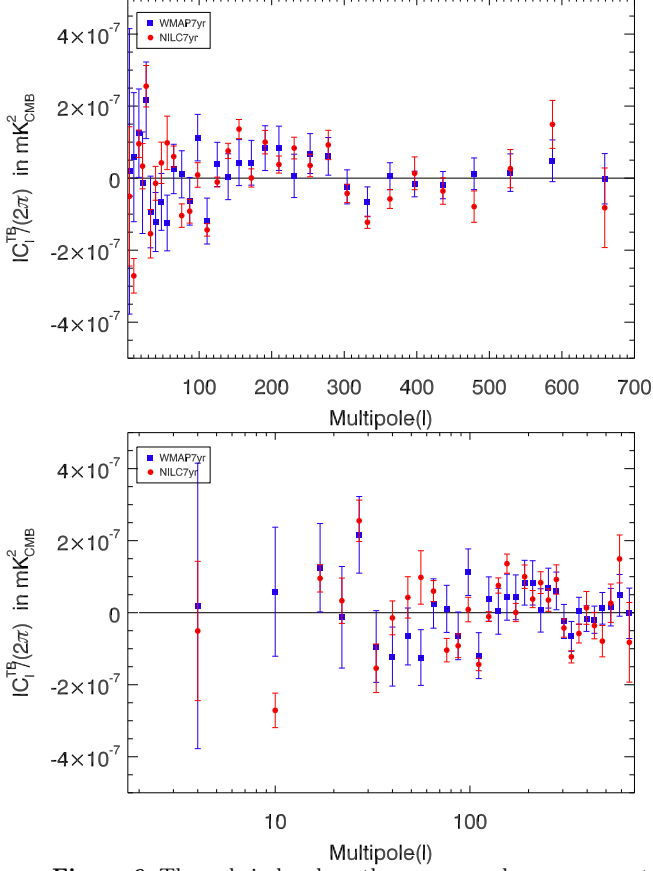**Figure 6.** The red circles show the cross-angular power spectrum of CMB temperature anisotropies (T-mode) and B-mode of CMB polarisation estimated using 7 years of observation of WMAP. The dark blue squares show the 7-year angular power spectrum of E-mode of CMB polarisation published by the WMAP collaboration. The top panel uses a linear scale in the horizontal axis, and the bottom panel a logarithmic scale.

Figure 7. The red circles show the cross-angular power spectrum of E-mode and B-mode of CMB polarisation estimated using 7 years of observations of WMAP. The top panel uses a linear scale in the horizontal axis, and the bottom panel a logarithmic scale. We use the same legend and color code for data points in this figures as in Figs. 5, 6 and 8, although WMAP data points are absent here.

departure from zero (few sigma) (see table 4). This discrepancy between model and measurement, although small, is presently not fully understood, although a possible explanation is effects of beam imperfections, inducing a leakage of T into B (see, e.g., Kaplan & Delabrouille 2002; Hu, Hedman, & Zaldarriaga 2003; Rosset et al. 2007, for discussions of such effects). A detailed investigation of these discrepancies requires very accurate modelling of the measurement and of the data processing pipeline, and is beyond the scope of the present paper.

4.5.4   EB cross-spectrum

The WMAP collaboration has not provided cross-angular power spectra for E and B-modes of CMB polarisation. Our estimated EB cross-power spectrum, displayed in figure 7 and tabulated in table 5, is compatible with zero as expected from the current cosmological best-fit model.

4.5.5   BB angular power spectrum

Finally, the power spectrum of CMB B-modes is of special interest, as it provides one of the most promising means of
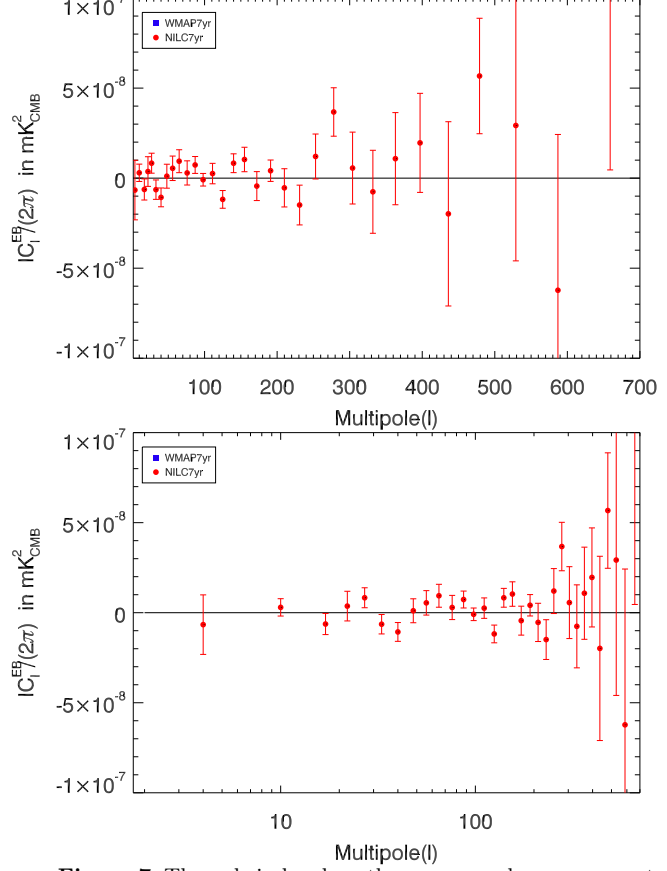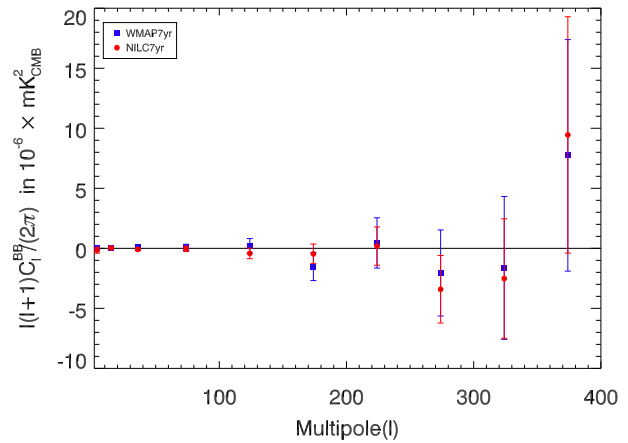

Figure 8. The red circles show the angular power spectrum of B-mode of CMB polarisation estimated using 7 years of observations of WMAP. The dark blue squares show the 7-year angular power spectrum of E-mode of CMB polarisation published by the WMAP collaboration.

Table 4. Comparison of our estimate of binned cross-angular power spectrum of CMB temperature anisotropies (T-mode) and B-mode of CMB polarisation with that provided by WMAP team. The quantities tabulated are $D'_l = lC_l^{TB}/2\pi$ and $\Delta D'_l = l\Delta C_l^{TB}/2\pi$.

l	$D_l^{',\mathrm{nilc}}$	$D_l^{',\mathrm{wmap}}$	$\Delta D_l^{',\mathrm{nilc}}$	$\Delta D_l^{',\mathrm{wmap}}$
	(mK^2)	(mK^2)	(mK^2)	(mK^2)
4	-5.067e-08	1.886e-08	1.934e-07	3.964e-07
10	-2.712e-07	5.827e-08	4.792e-08	1.792e-07
17	9.538e-08	1.248e-07	3.799e-08	1.227e-07
22	3.318e-08	-1.271e-08	6.299e-08	1.411e-07
27	2.552e-07	2.161e-07	5.745e-08	1.064e-07
33	-1.543e-07	-9.393e-08	6.736e-08	9.954e-08
40	-1.438e-08	-1.218e-07	4.705e-08	8.194e-08
48	4.251e-08	-6.598e-08	5.740e-08	7.899e-08
56	9.792e-08	-1.244e-07	7.419e-08	7.735e-08
65	5.989e-08	2.553e-08	2.932e-08	6.850e-08
76	-1.040e-07	1.068e-08	3.258e-08	6.537e-08
87	-9.185e-08	-6.428e-08	3.301e-08	6.613e-08
98	8.777e-09	1.124e-07	3.412e-08	6.460e-08
111	-1.437e-07	-1.192e-07	1.734e-08	6.379e-08
125	-1.088e-08	3.799e-08	1.358e-08	6.145e-08
140	7.557e-08	4.004e-09	2.116e-08	6.374e-08
155	1.362e-07	4.314e-08	2.662e-08	6.390e-08
172	5.176e-10	4.273e-08	2.524e-08	6.220e-08
191	9.992e-08	8.331e-08	3.258e-08	6.215e-08
210	3.781e-08	8.273e-08	2.373e-08	6.153e-08
231	8.348e-08	6.303e-09	3.015e-08	6.018e-08
253	3.510e-08	6.825e-08	3.120e-08	5.542e-08
278	9.221e-08	6.048e-08	4.072e-08	5.225e-08
304	-4.245e-08	-2.426e-08	2.556e-08	4.731e-08
332	-1.225e-07	-6.575e-08	1.695e-08	4.148e-08
363	-5.776e-08	5.235e-09	2.630e-08	3.751e-08
397	1.339e-08	-1.634e-08	4.559e-08	3.550e-08
436	-3.581e-08	-1.947e-08	3.669e-08	3.777e-08
479	-7.900e-08	1.212e-08	4.362e-08	4.400e-08
529	2.633e-08	1.537e-08	5.317e-08	5.208e-08
587	1.492e-07	4.820e-08	6.660e-08	5.796e-08
659	-8.227e-08	-1.772e-09	1.105e-07	6.992e-08

Table 5. Our estimate of binned cross-angular power spectrum of E-mode and B-mode of CMB polarisation. The quantities tabulated are $D'_l = lC_l^{EB}/2\pi$ and $\Delta D'_l = l\Delta C_l^{EB}/2\pi$.

l	$D_l^{',\mathrm{nilc}}$	$\Delta D_l^{',\mathrm{nilc}}$
	(mK^2)	(mK^2)
4	-6.628e-09	1.653e-08
10	2.959e-09	4.820e-09
17	-6.286e-09	5.869e-09
22	3.663e-09	8.229e-09
27	8.301e-09	5.535e-09
33	-6.395e-09	5.399e-09
40	-1.068e-08	5.223e-09
48	1.074e-09	6.654e-09
56	5.471e-09	6.788e-09
65	9.406e-09	6.366e-09
76	2.895e-09	6.717e-09
87	7.319e-09	4.688e-09
98	-8.880e-10	3.486e-09
111	2.534e-09	5.676e-09
125	-1.179e-08	4.923e-09
140	8.282e-09	5.222e-09
155	1.036e-08	6.794e-09
172	-4.414e-09	8.033e-09
191	4.128e-09	5.939e-09
210	-5.390e-09	1.062e-08
231	-1.493e-08	1.104e-08
253	1.203e-08	1.248e-08
278	3.674e-08	1.345e-08
304	5.604e-09	1.995e-08
332	-7.582e-09	2.305e-08
363	1.081e-08	2.559e-08
397	1.959e-08	2.750e-08
436	-1.982e-08	5.117e-08
479	5.673e-08	3.206e-08
529	2.924e-08	7.517e-08
587	-6.226e-08	8.651e-08
659	1.338e-07	1.293e-07

Table 6. Comparison of our estimate of binned angular power spectrum of B-mode of CMB polarisation, with that provided by WMAP team. The quantities tabulated are $D_l = l(l+1)C_l^{BB}/2\pi$ and $\Delta D_l = l(l+1)\Delta C_l^{BB}/2\pi$.

l	D_l^{nilc}	D_l^{wmap}	$\Delta D_l^{\mathrm{nilc}}$	$\Delta D_l^{\mathrm{wmap}}$
	(mK^2)	(mK^2)	(mK^2)	(mK^2)
4	-1.539e-07	1.672e-09	2.466e-07	2.943e-08
15	2.947e-08	2.623e-08	7.861e-08	5.700e-08
36	-9.478e-08	1.437e-07	1.055e-07	1.248e-07
74	-4.331e-08	7.960e-08	2.272e-07	2.560e-07
124	-4.248e-07	2.177e-07	4.432e-07	5.966e-07
174	-4.622e-07	-1.519e-06	8.142e-07	1.165e-06
224	1.858e-07	4.507e-07	1.594e-06	2.092e-06
274	-3.411e-06	-2.052e-06	2.811e-06	3.581e-06
324	-2.517e-06	-1.631e-06	4.979e-06	5.952e-06
374	9.446e-06	7.744e-06	9.846e-06	9.643e-06

detecting primordial tensor modes in the early universe, and constrain models of inflation. Significant effort is currently undertaken to prepare the measurement of B-modes with a future space mission. One such mission, the Cosmic Origins Explorer (COrE), has been proposed to ESA within Cosmic Vision 2015-2025 (The COrE Collaboration et al. 2011). Missions with similar objectives, but different designs, have been proposed to NASA (see, e.g., Baumann et al. 2009). Contamination by foregrounds is one of the main worries for this measurement, and the investigation of the severeness of the contamination, as well as the development and validation of component separation methods adapted to the challenge of measuring CMB B-modes, has focused significant attention recently (Tucci et al. 2005; Stivoli et al. 2006; Amblard, Cooray, & Kaplinghat 2007; Betoule et al. 2009; Dunkley et al. 2009; Efstathiou, Gratton, & Paci 2009; Stivoli et al. 2010).

Clearly, the WMAP mission lacks the sensitivity to place a meaningful limit on the B-mode polarisation. As expected, neither our result nor that of the WMAP collab-

oration[4] do show any detection of *B*-modes (see figure 8 and table 6). The method used in the present paper, however, has been also tested on realistic simulations of future observations with COrE. On such simulations, it allows to reject foreground contamination effectively enough to measure tensor to scalar ratio of 10^{-3}, limited by the sensitivity of the observations rather than foreground contamination.

5 CONCLUSIONS:

Following our previous work on WMAP temperature maps, we have computed CMB power spectra for polarised WMAP observations. CMB polarisation maps for *T*, *E*, and *B* are obtained from WMAP observations using linear combinations that minimize the variance of the recovered CMB on wavelet (needlet) domains (the Needlet ILC method), that are subsequently used to compute CMB power spectra.

Our analysis differs substantially from that of the WMAP team: we use all WMAP channels, use a needlet ILC over the full range of harmonic modes, and produce 7 independent maps for each of *T*, *E* and *B*, from the different years of observation. Error bars do not rely on a model of the WMAP noise, but instead are computed directly from the internal scatter of all possible (21 in our case) independent band-averaged cross-spectra.

We find that our *EE* power spectrum is in excellent agreement with the expectations from the current 'concordance' cosmological model, while the 7-year WMAP spectrum publicly available on the Lambda web site[5] seems to be systematically higher. Our statistical error bars on *EE* are lower comparable to those of the published WMAP result in most of the multipole bins under consideration (and are, actually, 10-20% lower on average, except for the first bin). On *TE* and *TB*, our error bars are also smaller than the WMAP ones, but we note that a few data points deviate by few sigma from the expected best-fit value, a feature that will need to be investigated with future data sets. Finally, our measurements of the *EB* and *BB* spectra are compatible with zero.

REFERENCES

Amblard A., Cooray A., Kaplinghat M., 2007, PhRvD, 75, 083508

Astier P., et al., 2006, A&A, 447, 31

Baker J. C., et al., 1999, MNRAS, 308, 1173

Basak S., Delabrouille J., 2012, MNRAS, 419, 1163

Baumann et al. (CMBPol Study Team), AIP Conf.Proc. 1141, 10 (2009), 0811.3919

Bennett C. L., et al., 1992, ApJ, 396, L7

Bennett C. L., et al., 1996, ApJ, 464, L1

Bennett C. L., et al., 2003, ApJS, 148, 1

Benoît A., et al., 2003, A&A, 399, L19

Benoît A., et al., 2003, A&A, 399, L25

Betoule M., Pierpaoli E., Delabrouille J., Le Jeune M., Cardoso J.-F., 2009, A&A, 503, 691

Bischoff C., et al., 2008, ApJ, 684, 771

Brown M. L., et al., 2009, ApJ, 705, 978

Chiang H. C., et al., 2010, ApJ, 711, 1123

The COrE Collaboration, et al., 2011, arXiv, arXiv:1102.2181

Das S., et al., 2011, ApJ, 729, 62

Das S., et al., 2011, PhRvL, 107, 021301

de Bernardis P., et al., 2000, Nature, 404, 955

Delabrouille J., Cardoso J.-F., 2009, LNP, 665, 159

Delabrouille J., Cardoso J.-F., Le Jeune M., Betoule M., Faÿ G., Guilloux F., 2009, A&A, 493, 835

Dick J., Remazeilles M., Delabrouille J., 2010, MNRAS, 401, 1602

Dickinson C., et al., 2004, MNRAS, 353, 732

Dunkley J., et al., 2009, AIPC, 1141, 222

Efstathiou G., Gratton S., Paci F., 2009, MNRAS, 397, 1355

Eisenstein D. J., et al., 2005, ApJ, 633, 560

Eriksen H. K., Banday A. J., Górski K. M., Lilje P. B., 2004, ApJ, 612, 633

Faÿ G., Guilloux F., Betoule M., Cardoso J.-F., Delabrouille J., Le Jeune M., 2008, PhRvD, 78, 083013

Finkbeiner D. P., 2003, ApJS, 146, 407

Freedman W. L., et al., 2001, ApJ, 553, 47

Goldberg J. N., Macfarlane A. J., Newman E. T., Rohrlich F., Sudarshan E. C. G., 1967, JMP, 8, 2155

Górski K. M., Hivon E., Banday A. J., Wandelt B. D., Hansen F. K., Reinecke M., Bartelmann M., 2005, ApJ, 622, 759

Guilloux F., Fay G., Cardoso J.-F., 2009, Appl. Comput. Harmon. Anal., 26, vol. 2, 143

Guy J., et al., 2010, A&A, 523, A7

Hanany S., et al., 2000, ApJ, 545, L5

Haslam C. G. T., Klein U., Salter C. J., Stoffel H., Wilson W. E., Cleary M. N., Cooke D. J., Thomasson P., 1981, A&A, 100, 209

Hu W., Hedman M. M., Zaldarriaga M., 2003, PhRvD, 67, 043004

Kamionkowski M., Kosowsky A., Stebbins A., 1997, PhRvD, 55, 7368

Kaplan J., Delabrouille J., 2002, AIPC, 609, 209

Keisler R., et al., 2011, ApJ, 743, 28

Larson D., et al., 2011, ApJS, 192, 16

Leitch E. M., Kovac J. M., Halverson N. W., Carlstrom J. E., Pryke C., Smith M. W. E., 2005, ApJ, 624, 10

Marinucci D., et al., 2008, MNRAS, 383, 539

---

[4] http://lambda.gsfc.nasa.gov/data/map/dr4/dcp/spectra/wmap_bb_spectrum_7yr_v4p1.txt

[5] http://lambda.gsfc.nasa.gov/

Montroy T. E., et al., 2006, ApJ, 647, 813

Narcowich, F. Petrushev, P. and Ward, 2006, J., SIAM J. Math. Anal. 38, vol. 2, 574

Nolta M. R., et al., 2009, ApJS, 180, 296

Pearson T. J., et al., 2003, ApJ, 591, 556

Perlmutter S., et al., 1999, ApJ, 517, 565

Piacentini F., et al., 2006, ApJ, 647, 833

Pietrobon D., Amblard A., Balbi A., Cabella P., Cooray A., Marinucci D., 2008, PhRvD, 78, 103504

Pryke C., et al., 2009, ApJ, 692, 1247

QUIET Collaboration, et al., 2011, ApJ, 741, 111

Rebolo R., et al., 2004, MNRAS, 353, 747

Rees M. J., 1968, ApJ, 153, L1

Reichardt C. L., et al., 2009, ApJ, 694, 1200

Rosset C., Yurchenko V. B., Delabrouille J., Kaplan J., Giraud-Héraud Y., Lamarre J.-M., Murphy J. A., 2007, A&A, 464, 405

Rudjord Ø., Hansen F. K., Lan X., Liguori M., Marinucci D., Matarrese S., 2009, ApJ, 701, 369

Saha, R., 2011,ApJL, 739, L56

Saha R., Jain P., Souradeep T., 2006, ApJ, 645, L89

Saha R., Prunet S., Jain P., Souradeep T., 2008, Phys. Rev. D, 78, 023003

Samal P. K., Saha R., Delabrouille J., Prunet S., Jain P., Souradeep T., 2010,. ApJ, 714, 840

Schlegel D. J., Finkbeiner D. P., Davis M., 1998, ApJ, 500, 525

Seljak U., Slosar A., McDonald P., 2006, JCAP, 10, 14

Sievers J. L., et al., 2007, ApJ, 660, 976

Stivoli F., Baccigalupi C., Maino D., Stompor R., 2006, MNRAS, 372, 615

Souradeep T., 2011, Bull. Astron. Soc. India, 39, 163

Souradeep T., Saha R., Jain P., 2006, Nat, 50, 854

Stivoli F., Grain J., Leach S. M., Tristram M., Baccigalupi C., Stompor R., 2010, MNRAS, 408, 2319

Tegmark M., 1998, ApJ, 502, 1

Tegmark, M., de Oliveira-Costa, A., Hamilton, A. J. S., Phys. Rev. D 68 (2003), 123523

Tucci M., Martínez-González E., Vielva P., Delabrouille J., 2005, MNRAS, 360, 935

Wu J. H. P., et al., 2007, ApJ, 665, 55

Zaldarriaga M., Seljak U., 1997, PhRvD, 55, 1830